Theoretical and Applied Fracture Mechanics 108 (2020) 102573

Contents lists available at ScienceDirect

Theoretical and Applied Fracture Mechanics

journal homepage: www.elsevier.com/locate/tafmec

A coupling model of XFEM/peridynamics for 2D dynamic crack propagation and branching problems

Shuo Liu[a], Guodong Fang[a,*], Jun Liang[b,*], Dongkai Lv[c]

[a] Science and Technology on Advanced Composites in Special Environment Key Laboratory, Harbin Institute of Technology, Harbin 150001, PR China
[b] Institute of Advanced Structure Technology, Beijing Institute of Technology, Beijing 100081, PR China
[c] Metrology Testing Center, China Academy of Engineering Physics, Mianyang 621900, PR China

ARTICLE INFO

Keywords:
Peridynamics
Coupling
Dynamic crack propagation
Extended finite element method

ABSTRACT

Peridynamics (PD) and extended finite element method (XFEM) are coupled in the explicit integration scheme to study the 2D dynamic fracture problems. The advantages of PD for the crack propagation and XFEM for the strong displacement discontinuity description of the crack are combined together. The proposed method can improve the computation efficiency in comparison of the pure PD, and can avoid using macroscopic criteria to judge the crack propagation orientation of XFEM. The coupling scheme for the stiffness and mass matrices of PD and XFEM is given in the coupling region. The horizon length δ is examined to study their influences on the convergence of the proposed method. The accuracy of the dynamic fracture simulation using the proposed method is also validated in comparison of experimental and other numerical methods.

1. Introduction

Crack initiation and propagation problems can be simulated using some numerical methods, for instance meshless method [1], boundary element method [2], particle method [3], finite element method (FEM) and extended finite element method (XFEM) etc. [4,5]. Recently, peridynamics (PD) as a non-local theory has been proposed, integro-differential equations rather than differential equations are used in PD and this characteristic make it easy to study the discontinuous problems without any additional processing [6–12]. PD has been used to study the quasi-static crack propagation [13–18], dynamic crack propagation [19–28], and impact failure [29,30], etc. In addition, PD theory has been improved by many scholars, such as peridynamic differential operator [31] and unified the local and nonlocal models [32,33]. However, the computational efficiency of PD is lower than that of the numerical methods based on local theory (such as FEM, XFEM and meshless finite node method, etc.) [34–39].

Some coupling schemes, such as force-based coupling method [36,37], displacement-based coupling method [35,38,39], sub-modeling method [40,41] and morphing method [42–47], etc., were proposed to couple PD and numerical methods based on local theory in the past few years. Oterkus [40,41] presented a sub-model method to couple FEM and PD, in which the global model is discretized by FEM and the sub-model is discretized by PD to simulate the damage prediction. Refs. [42–47] using the mixed function method to achieve the coupling of the local model and the nonlocal model. Refs. [48–50] proposed a coupling FEM and PD method, in which doesn't include the overlapping region. Zaccariotto [51] also used the above coupling method to study quasi-static and dynamic crack growth problems. It should be noted that no attempt is made to couple XFEM and PD in the open literatures. XFEM can supplement the disadvantage of traditional FEM solving discontinuous deformation problems [52–54]. However, XFEM encounters troubles when handle with multi-cracks, crack bifurcation problems and 3-D crack propagations [27,48]. These disadvantages for XFEM might be avoided by combining with PD.

In this paper, a coupling scheme between XFEM and PD is proposed to exert the advantages of these two methods for 2D crack propagation and branching problems. The crack tip and expected crack propagation regions are modeled by PD, while the initial crack excluding crack tip region and the other region are performed using XFEM. The stiffness matrix, mass matrix and time integration scheme of the coupling method are all provided in detail. It's worth noting that the coupling method might be extended to the 3D problems to simulate 3D crack propagation and branching, which is a challenging job for XFEM.

2. Theory of bond-based PD

The discrete form of the motion equation of bond-based PD can be written as [55]

* Corresponding authors.
E-mail addresses: fanggd@hit.edu.cn (G. Fang), liangjun@bit.edu.cn (J. Liang).

https://doi.org/10.1016/j.tafmec.2020.102573
Received 2 December 2019; Received in revised form 3 January 2020; Accepted 9 March 2020
Available online 12 March 2020
0167-8442/ © 2020 Elsevier Ltd. All rights reserved.

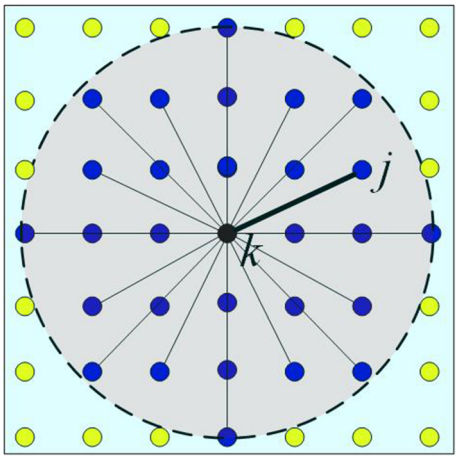

Fig. 1. Generic horizon of node k.

$$\rho_k \ddot{\mathbf{u}}_k = \sum_{j=1}^{N} \mathbf{f}_{kj}(\mathbf{u}_j, \mathbf{u}_k, \mathbf{x}_j, \mathbf{x}_k, t)V_j + \mathbf{b}_k(\mathbf{x}, t) \tag{1}$$

where $\mathbf{u}_k$, $\mathbf{u}_j$ and $\mathbf{x}_k$, $\mathbf{x}_j$ are displacements and coordinates of nodes k and j. $\mathbf{b}_k$ denotes a prescribed body-force density field. $\mathbf{f}_{kj}$ is the pair-wise force function. N denotes the total number of material nodes that within the family of the node k (gray region) as displayed in Fig. 1. V_j represents the volume of node j. ρ_k and t are the material density of node k and time.

For small displacements condition, the pair-wise force function of the Prototype Microelatic Brittle (PMB) material [6,7,34] is defined as

$$\mathbf{f}_{kj} = c(\boldsymbol{\xi}) s_{kj} \mu_{kj} \frac{\boldsymbol{\xi}}{|\boldsymbol{\xi}|}, \tag{2}$$

where $\boldsymbol{\xi} = \mathbf{x}_j - \mathbf{x}_k$. The bond-breaking parameterμ_{kj}denotes the status of the bond,

$$\mu_{kj} = \begin{cases} 1 & \text{for an active bond} \\ 0 & \text{for a broken bond} \end{cases} \tag{3}$$

For plane stress condition, the micro modulus $c(\boldsymbol{\xi})$ can be written as

$$c(\boldsymbol{\xi}) = c_0 = \frac{6E}{\pi h \delta^3 (1-\nu)}, \tag{4}$$

where δ is the horizon length and h denotes the thick of the plane.

s_{kj} is the bond stretch, which can be defined as

$$s_{kj} = \frac{|\boldsymbol{\eta} - \boldsymbol{\xi}| - |\boldsymbol{\xi}|}{|\boldsymbol{\xi}|}, \tag{5}$$

where $\boldsymbol{\eta} = \mathbf{u}_j - \mathbf{u}_k$.

If

$$s_{kj} \geqslant s_c, \tag{6}$$

the bond will be broken. s_c is the critical stretch, which is denoted by Eq. (7) for 2D isotropic and brittle materials [34]

$$s_c = \sqrt{\frac{4\pi G_c}{9E\delta}}, \tag{7}$$

where G_c represents the energy release rate.

Then the crack path is denoted by the PD nodes damage,

$$\phi_k = 1 - \frac{\sum_{j=1}^{N_k} \mu_{kj}}{N_k}. \tag{8}$$

By substituting Eq. (2) into Eq. (1), the PD equation can be rewritten as the matrix form

$$\rho_k \ddot{\mathbf{u}}_k V_k + \sum_{j=1}^{N} \mu_{kj}(\mathbf{k}_{kj}^{11}\mathbf{u}_k + \mathbf{k}_{kj}^{12}\mathbf{u}_j) = \mathbf{b}_k V_k, \tag{9}$$

where $\mathbf{k}_{kj}^{11}$ and $\mathbf{k}_{kj}^{12}$ are written as [34]

$$\mathbf{k}_{kj}^{PD} = \frac{c_0 V_k V_j}{|\boldsymbol{\xi}|} \left[\begin{array}{cc|cc} \xi_1^2 & \xi_1\xi_2 & -\xi_1^2 & -\xi_1\xi_2 \\ \xi_1\xi_2 & \xi_2^2 & -\xi_1\xi_2 & -\xi_2^2 \end{array}\right] = \left[\mathbf{k}_{kj}^{11} \quad \mathbf{k}_{kj}^{12}\right]. \tag{10}$$

According to Ref. [51], the motion equation of PD nodes can be written in FEM form

$$\mathbf{M}_{PD}\ddot{\boldsymbol{\delta}}_{PD} + \mathbf{K}_{PD}\boldsymbol{\delta}_{PD} = \mathbf{R}_{PD}, \tag{11}$$

where $\mathbf{M}_{PD}$ and $\mathbf{K}_{PD}$ denote the lumped mass matrix and the global stiffness matrix, respectively. $\boldsymbol{\delta}_{PD}$ represents the displacement vector of all PD nodes, and $\mathbf{R}_{PD}$ is the loading vector of all PD nodes.

3. Overview of XFEM

As for a small deformation domain with initial crack under dynamic loading, the governing equation and boundary condition are [4]

$$\sigma_{ij,j} + b_i = \rho \ddot{u}_i, \tag{12}$$

$$\sigma_{ij} n_j = \bar{t}_i \quad \text{on } S_\sigma, \tag{13}$$

$$u_i = \bar{u}_i \quad \text{on } S_u, \tag{14}$$

where $\sigma_{ij}$is the Cauchy's stress tensor, $b_i$represents the body force density. $\bar{t}_i$ and $\bar{u}_i$ are the surface force and the displacement on the boundary S ($S = S_\sigma + S_u$). ρ denotes material density. n_j is the normal unit vector on the boundary S_σ.

The initial condition is written as

$$u_i(x, t=0) = \bar{u}_i(0), \tag{15}$$

$$\dot{u}_i(x, t=0) = \bar{\dot{u}}_i(0). \tag{16}$$

The variational equation of this problem is [4]

$$\int_\Omega \sigma_{ij}\delta\varepsilon_{ij} d\Omega + \int_\Omega \rho \ddot{u}_i \delta u_i d\Omega = \int_\Omega b_i \delta u_i d\Omega + \int_\Gamma \bar{t}_i \delta u_i d\Gamma, \tag{17}$$

where ε_{ij} represents the strain tensor. The nodal displacement in the discrete domain can be written as [4,5]

$$\mathbf{u} = \sum_{i\in N^s} N_i(\mathbf{x})\mathbf{u}_i + \sum_{i\in N^{cut}} \bar{N}_i(\mathbf{x})[H(\mathbf{x}) - H(\mathbf{x}_i)]\mathbf{a}_i + \sum_{i\in N^{tip}} \bar{N}_i(\mathbf{x}) \sum_j [B_j(\mathbf{x}) - B_j(\mathbf{x}_i)]\mathbf{b}_i^j, \tag{18}$$

where N^s is the nodal set in the discrete domain. N^i and $\mathbf{u}_i$ denote the shape function and the nodal displacement of the node i, respectively. N^{cut} is the shape function of the nodal set of nodes for completely cut elements. The nodes in the crack-crossed elements are expressed by circles in Fig. 2. $\bar{N}_i(\mathbf{x})$ and $H(\mathbf{x})$ are the partition of unity function and Heaviside step function. $\mathbf{a}_i$ represents enrichment variables of nodes in the completely cut elements. N^{tip} is the shape function of the nodal set for the partially cut element. The nodes of crack-embedded elements are expressed using square in Fig. 2. $B_j(x)$ is the crack tip enrichment

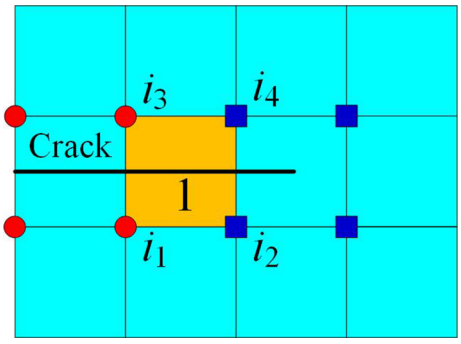

Fig. 2. Enriched schemes of nodes in the crack-cut element.

function, and $\mathbf{b}_i^j$ denotes enrichment variables of nodes of the partially cut element.

The motion equation of XFEM can be obtained by Bubnov-Galerkin method regardless of the damping [4].

$$\mathbf{M}_{XFEM}\ddot{\boldsymbol{\delta}}_{XFEM} + \mathbf{K}_{XFEM}\boldsymbol{\delta}_{XFEM} = \mathbf{F}_{XFEM}, \tag{19}$$

where $\boldsymbol{\delta}_{XFEM}$ is the nodal displacement vector, and $\mathbf{F}_{XFEM}$ represents the load vector. $\mathbf{K}_{XFEM}$ and $\mathbf{M}_{XFEM}$ denote the global stiffness matrix and lumped mass matrix. The global stiffness matrix is assembled by all element stiffness matrices in the computation domain. The element stiffness matrix of element 1 as shown in Fig. 2 can be written as

$$\mathbf{k}_{ij}^{e} = \begin{bmatrix} \mathbf{k}_{ij}^{uu} & \mathbf{k}_{ij}^{ua} & \mathbf{k}_{ij}^{ub} \\ \mathbf{k}_{ij}^{au} & \mathbf{k}_{ij}^{aa} & \mathbf{k}_{ij}^{ab} \\ \mathbf{k}_{ij}^{bu} & \mathbf{k}_{ij}^{ba} & \mathbf{k}_{ij}^{bb} \end{bmatrix} \quad (i = i_1, i_2, i_3, i_4, j = i_1, i_2, i_3, i_4). \tag{20}$$

The details of the element stiffness matrix are displayed in Ref. [4].

The lumped mass matrices of XFEM are difficult to be obtained because the enrichment variables of nodes does not have physical meaning. A lumped mass matrix for the enriched element is introduced in Ref. [56] to use the explicit formulation of XFEM. The diagonal coefficient corresponding to the lumped mass matrix of the enrichment variables is written as

$$\mathbf{m}_{diag} = \frac{m_{element}}{n_{nodes}} \frac{1}{V} \int_V H^2 dV, \tag{21}$$

where m_{element} and n_{nodes} represent the mass and total node number of the element. V is the element volume.

The lumped mass matrix is assembled by all element mass matrices of the computation domain. The element mass matrix of element 1 as seen in Fig. 2 can be written as [4]

$$\mathbf{m}_i^e = \begin{bmatrix} \mathbf{m}_i^u & \mathbf{0} & \mathbf{0} \\ \mathbf{0} & \mathbf{m}_i^a & \mathbf{0} \\ \mathbf{0} & \mathbf{0} & \mathbf{m}_i^b \end{bmatrix} \quad (i = i_1, i_2, i_3, i_4, j = i_1, i_2, i_3, i_4). \tag{22}$$

4. Coupling XFEM and PD

The computation domain for 2D crack propagation problem can be divided into several regions for coupling method of XFEM/PD. The region contains the crack tip and the region has potential to crack propagation are studied using PD. The region with initial crack excluding the crack tip can be modeled using XFEM. Thus, combining with the advantages of XFEM and PD, the computation domain with an initial crack is divided into the PD region Ω_1, the coupling region Ω_2 and the XFE region Ω_3 as displayed in Fig. 3. The coupling region is between the XFE region and the PD region, which includes the XFE nodes and PD material nodes. For simplicity, the uniform node spacing is used in this study.

To adopt the explicit integration scheme, the mass and stiffness matrices should be determined for the coupling model of PD/XFEM. In the PD region, stiffness and mass matrices are the same as general PD given in Section 2. For example, the stiffness of PD node a_1 that shown in Fig. 3(a) interacting with any node a_n within its horizon can be written as

$$\mathbf{k}_{a_1a_n}^{PD} = \frac{c_0 V_{a_1} V_{a_n}}{|\boldsymbol{\xi}|} \left[\begin{array}{cc:cc} \xi_1^2 & \xi_1\xi_2 & -\xi_1^2 & -\xi_1\xi_2 \\ \xi_1\xi_2 & \xi_2^2 & -\xi_1\xi_2 & -\xi_2^2 \\ \hdashline -\xi_1^2 & -\xi_1\xi_2 & \xi_1^2 & \xi_1\xi_2 \\ -\xi_1\xi_2 & -\xi_2^2 & \xi_1\xi_2 & \xi_2^2 \end{array}\right] = \left[\begin{array}{c:c} \mathbf{k}_{a_1a_n}^{11} & \mathbf{k}_{a_1a_n}^{12} \\ \hdashline \mathbf{k}_{a_1a_n}^{21} & \mathbf{k}_{a_1a_n}^{22} \end{array}\right], \tag{23}$$

where $\xi_1 = \frac{x_{an} - x_{a1}}{|\xi|}$, $\xi_2 = \frac{y_{an} - y_{a1}}{|\xi|}$.

The mass matrix of PD node a_1 can be written as

$$\mathbf{m}_{a_1} = \begin{bmatrix} \rho V_{a_1} & 0 \\ 0 & \rho V_{a_1} \end{bmatrix}, \tag{24}$$

where ρ and V_i represent material density and volume of PD node a_1.

In the XFE region, the stiffness matrix for general elements and enrichment elements have the different forms. The stiffness and mass matrices for XFEM are derived in Section 3. For example, the stiffness matrix of element 1, element 2 and element 3 as shown in Fig. 3(b) can be written as Eqs. (25)–(27), respectively.

$$\mathbf{k}_{b_5b_6b_8b_7}^{e} = \begin{bmatrix} \mathbf{k}_{b_5b_5}^{uu} & \mathbf{k}_{b_5b_6}^{uu} & \mathbf{k}_{b_5b_8}^{uu} & \mathbf{k}_{b_5b_7}^{uu} & \mathbf{k}_{b_5b_5}^{ua} & \mathbf{k}_{b_5b_6}^{ua} & \mathbf{k}_{b_5b_8}^{ua} & \mathbf{k}_{b_5b_7}^{ua} \\ \mathbf{k}_{b_6b_5}^{uu} & \mathbf{k}_{b_6b_6}^{uu} & \mathbf{k}_{b_6b_8}^{uu} & \mathbf{k}_{b_6b_7}^{uu} & \mathbf{k}_{b_6b_5}^{ua} & \mathbf{k}_{b_6b_6}^{ua} & \mathbf{k}_{b_6b_8}^{ua} & \mathbf{k}_{b_6b_7}^{ua} \\ \mathbf{k}_{b_8b_5}^{uu} & \mathbf{k}_{b_8b_6}^{uu} & \mathbf{k}_{b_8b_8}^{uu} & \mathbf{k}_{b_8b_7}^{uu} & \mathbf{k}_{b_8b_5}^{ua} & \mathbf{k}_{b_8b_6}^{ua} & \mathbf{k}_{b_8b_8}^{ua} & \mathbf{k}_{b_8b_7}^{ua} \\ \mathbf{k}_{b_7b_5}^{uu} & \mathbf{k}_{b_7b_6}^{uu} & \mathbf{k}_{b_7b_8}^{uu} & \mathbf{k}_{b_7b_7}^{uu} & \mathbf{k}_{b_7b_5}^{ua} & \mathbf{k}_{b_7b_6}^{ua} & \mathbf{k}_{b_7b_8}^{ua} & \mathbf{k}_{b_7b_7}^{ua} \\ \mathbf{k}_{b_5b_5}^{au} & \mathbf{k}_{b_5b_6}^{au} & \mathbf{k}_{b_5b_8}^{au} & \mathbf{k}_{b_5b_7}^{au} & \mathbf{k}_{b_5b_5}^{aa} & \mathbf{k}_{b_5b_6}^{aa} & \mathbf{k}_{b_5b_8}^{aa} & \mathbf{k}_{b_5b_7}^{aa} \\ \mathbf{k}_{b_6b_5}^{au} & \mathbf{k}_{b_6b_6}^{au} & \mathbf{k}_{b_6b_8}^{au} & \mathbf{k}_{b_6b_7}^{au} & \mathbf{k}_{b_6b_5}^{aa} & \mathbf{k}_{b_6b_6}^{aa} & \mathbf{k}_{b_6b_8}^{aa} & \mathbf{k}_{b_6b_7}^{aa} \\ \mathbf{k}_{b_8b_5}^{au} & \mathbf{k}_{b_8b_6}^{au} & \mathbf{k}_{b_8b_8}^{au} & \mathbf{k}_{b_8b_7}^{au} & \mathbf{k}_{b_8b_5}^{aa} & \mathbf{k}_{b_8b_6}^{aa} & \mathbf{k}_{b_8b_8}^{aa} & \mathbf{k}_{b_8b_7}^{aa} \\ \mathbf{k}_{b_7b_5}^{au} & \mathbf{k}_{b_7b_6}^{au} & \mathbf{k}_{b_7b_8}^{au} & \mathbf{k}_{b_7b_7}^{au} & \mathbf{k}_{b_7b_5}^{aa} & \mathbf{k}_{b_7b_6}^{aa} & \mathbf{k}_{b_7b_8}^{aa} & \mathbf{k}_{b_7b_7}^{aa} \end{bmatrix}, \tag{25}$$

$$\mathbf{k}_{b_3b_4b_6b_5}^{e} = \begin{bmatrix} \mathbf{k}_{b_3b_3}^{uu} & \mathbf{k}_{b_3b_4}^{uu} & \mathbf{k}_{b_3b_6}^{uu} & \mathbf{k}_{b_3b_5}^{uu} & \mathbf{k}_{b_3b_6}^{ua} & \mathbf{k}_{b_3b_5}^{ua} \\ \mathbf{k}_{b_4b_3}^{uu} & \mathbf{k}_{b_4b_4}^{uu} & \mathbf{k}_{b_4b_6}^{uu} & \mathbf{k}_{b_4b_5}^{uu} & \mathbf{k}_{b_4b_6}^{ua} & \mathbf{k}_{b_4b_5}^{ua} \\ \mathbf{k}_{b_6b_3}^{uu} & \mathbf{k}_{b_6b_4}^{uu} & \mathbf{k}_{b_6b_6}^{uu} & \mathbf{k}_{b_6b_5}^{uu} & \mathbf{k}_{b_6b_6}^{ua} & \mathbf{k}_{b_6b_5}^{ua} \\ \mathbf{k}_{b_5b_3}^{uu} & \mathbf{k}_{b_5b_4}^{uu} & \mathbf{k}_{b_5b_6}^{uu} & \mathbf{k}_{b_5b_5}^{uu} & \mathbf{k}_{b_5b_6}^{ua} & \mathbf{k}_{b_5b_5}^{ua} \\ \mathbf{k}_{b_6b_3}^{au} & \mathbf{k}_{b_6b_4}^{au} & \mathbf{k}_{b_6b_6}^{au} & \mathbf{k}_{b_6b_5}^{au} & \mathbf{k}_{b_6b_6}^{aa} & \mathbf{k}_{b_6b_5}^{aa} \\ \mathbf{k}_{b_5b_3}^{au} & \mathbf{k}_{b_5b_4}^{au} & \mathbf{k}_{b_5b_6}^{au} & \mathbf{k}_{b_5b_5}^{au} & \mathbf{k}_{b_5b_6}^{aa} & \mathbf{k}_{b_5b_5}^{aa} \end{bmatrix}, \tag{26}$$

$$\mathbf{k}_{b_1b_2b_4b_3}^{e} = \begin{bmatrix} k_{b_1b_1}^{uu} & \mathbf{k}_{b_1b_2}^{uu} & \mathbf{k}_{b_1b_4}^{uu} & \mathbf{k}_{b_1b_3}^{uu} \\ \mathbf{k}_{b_2b_1}^{uu} & \mathbf{k}_{b_2b_2}^{uu} & \mathbf{k}_{b_2b_4}^{uu} & \mathbf{k}_{b_2b_3}^{uu} \\ \mathbf{k}_{b_4b_1}^{uu} & \mathbf{k}_{b_4b_2}^{uu} & \mathbf{k}_{b_4b_4}^{uu} & \mathbf{k}_{b_4b_3}^{uu} \\ \mathbf{k}_{b_3b_1}^{uu} & \mathbf{k}_{b_3b_2}^{uu} & \mathbf{k}_{b_3b_4}^{uu} & \mathbf{k}_{b_3b_3}^{uu} \end{bmatrix}. \tag{27}$$

where the superscript a represents enrichment variables of nodes in the completely cut elements. The superscript u is the displacement of nodes.

The mass matrix of element 1, element 2 and element 3 as displayed in Fig. 3(b) are represented by Eqs. (28)–(30),

$$\mathbf{m}_{b_5b_6b_8b_7}^{e} = \text{diag}\left\{\mathbf{m}_{b_5b_5}^{u}, \mathbf{m}_{b_6b_6}^{u}, \mathbf{m}_{b_8b_8}^{u}, \mathbf{m}_{b_7b_7}^{u}, \mathbf{m}_{b_5b_5}^{a}, \mathbf{m}_{b_6b_6}^{a}, \mathbf{m}_{b_8b_8}^{a}, \mathbf{m}_{b_7b_7}^{a}\right\}, \tag{28}$$

$$\mathbf{m}_{b_3b_4b_6b_5}^{e} = \text{diag}\left\{\mathbf{m}_{b_3b_3}^{u}, \mathbf{m}_{b_4b_4}^{u}, \mathbf{m}_{b_6b_6}^{u}, \mathbf{m}_{b_5b_5}^{u}, \mathbf{m}_{b_6b_6}^{a}, \mathbf{m}_{b_5b_5}^{a}\right\}, \tag{29}$$

$$\mathbf{m}_{b_1b_2b_4b_3}^{e} = \text{diag}\left\{\mathbf{m}_{b_1b_1}^{u}, \mathbf{m}_{b_2b_2}^{u}, \mathbf{m}_{b_4b_4}^{u}, \mathbf{m}_{b_3b_3}^{u}\right\}. \tag{30}$$

In the coupling region Ω_2, a PD node c_1 as shown in Fig. 3(a) can interact with all nodes, including PD nodes c_2 and XFE nodes d_1, d_2, in its horizon by using PD approach. The stiffness matrix of node c_1 and any node c_n in its horizon has the same formulation with Eq. (23), while the stiffness terms corresponding to the XFE nodal forces are set to zero.

$$\mathbf{k}_{c_1d_n}^{PD} = \frac{c_0 V_{c_1} V_{d_n}}{|\boldsymbol{\xi}|} \left[\begin{array}{cc:cc} \xi_1^2 & \xi_1\xi_2 & -\xi_1^2 & -\xi_1\xi_2 \\ \xi_1\xi_2 & \xi_2^2 & -\xi_1\xi_2 & -\xi_2^2 \\ \hdashline 0 & 0 & 0 & 0 \\ 0 & 0 & 0 & 0 \end{array}\right] = \left[\begin{array}{c:c} \mathbf{k}_{c_1d_n}^{11} & \mathbf{k}_{c_1d_n}^{12} \\ \hdashline \mathbf{0} & \mathbf{0} \end{array}\right]. \tag{31}$$

The mass matrices of the PD nodes in the coupling region have the same formulation with Eq. (24), which do not embody the interaction between other nodes (PD nodes and XFE nodes).

The nodes d_1, d_2, d_3 and d_4, as shown in Fig. 3(b), represents any XFE nodes in the region Ω_2. The XFE nodes in the region Ω_2 interact with all nodes around them, including PD nodes and XFE nodes, by XFEM approach. It should be noted that the interaction of a PD node to a XFE node is embodied in XFEM approach while the interaction of a XFE node to a PD node is obtained by PD approach. Thus, the stiffness and mass terms for the PD node in XFE are set to zero. To accurately

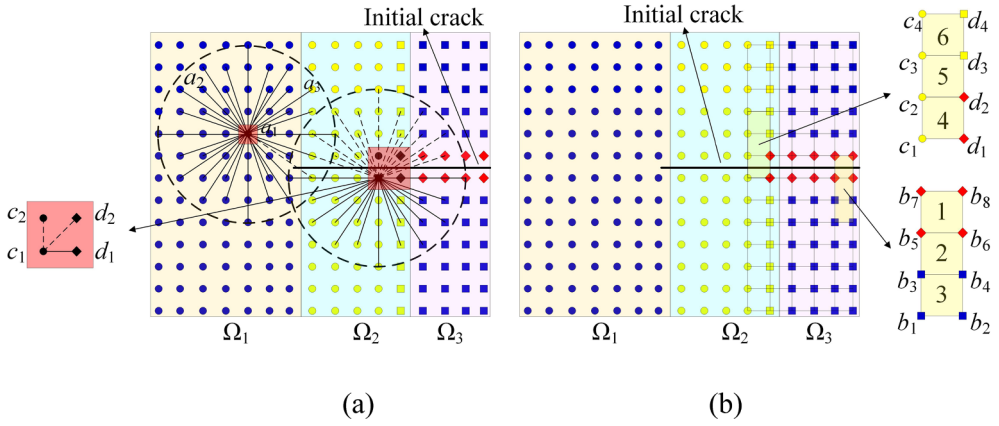

Fig. 3. A computation domain with an initial crack is divided into the PD region Ω_1, the coupling region Ω_2 and the XFE region Ω_3 (Circle, diamond and square nodes corresponding to PD nodes, XFE nodes close to crack and general XFE nodes, respectively). There are m layers PD nodes and 1 layer XFE nodes in region Ω_2.

describe the XFE nodal displacement, the stiffness terms for the XFE nodal force should include the contribution from the enrichment nodes (XFE nodes or PD nodes). As shown in Fig. 3(b), the element stiffness matrix of XFE 4, 5 and 6 are represented by Eqs. (32)–(34),

$$\mathbf{k}^e_{c_1d_1d_2c_2}=\begin{bmatrix}\mathbf{0} & \mathbf{0} & \mathbf{0} & \mathbf{0} & \mathbf{0} & \mathbf{0} & \mathbf{0} & \mathbf{0}\\ \mathbf{k}^{uu}_{d_1c_1} & \mathbf{k}^{uu}_{d_1d_1} & \mathbf{k}^{uu}_{d_1d_2} & \mathbf{k}^{uu}_{d_1c_2} & \mathbf{k}^{ua}_{d_1c_1} & \mathbf{k}^{ua}_{d_1d_1} & \mathbf{k}^{ua}_{d_1d_2} & \mathbf{k}^{ua}_{d_1c_2}\\ \mathbf{k}^{uu}_{d_2c_1} & \mathbf{k}^{uu}_{d_2d_1} & \mathbf{k}^{uu}_{d_2d_2} & \mathbf{k}^{uu}_{d_2c_2} & \mathbf{k}^{ua}_{d_2c_1} & \mathbf{k}^{ua}_{d_2d_1} & \mathbf{k}^{ua}_{d_2d_2} & \mathbf{k}^{ua}_{d_2c_2}\\ \mathbf{0} & \mathbf{0} & \mathbf{0} & \mathbf{0} & \mathbf{0} & \mathbf{0} & \mathbf{0} & \mathbf{0}\\ \mathbf{k}^{au}_{c_1c_1} & \mathbf{k}^{au}_{c_1d_1} & \mathbf{k}^{au}_{c_1d_2} & \mathbf{k}^{au}_{c_1c_2} & \mathbf{k}^{aa}_{c_1c_1} & \mathbf{k}^{aa}_{c_1d_1} & \mathbf{k}^{aa}_{c_1d_2} & \mathbf{k}^{aa}_{c_1c_2}\\ \mathbf{k}^{au}_{d_1c_1} & \mathbf{k}^{au}_{d_1d_1} & \mathbf{k}^{au}_{d_1d_2} & \mathbf{k}^{au}_{d_1c_2} & \mathbf{k}^{aa}_{d_1c_1} & \mathbf{k}^{aa}_{d_1d_1} & \mathbf{k}^{aa}_{d_1d_2} & \mathbf{k}^{aa}_{d_1c_2}\\ \mathbf{k}^{au}_{d_2c_1} & \mathbf{k}^{au}_{d_2d_1} & \mathbf{k}^{au}_{d_2d_2} & \mathbf{k}^{au}_{d_2c_2} & \mathbf{k}^{aa}_{d_2c_1} & \mathbf{k}^{aa}_{d_2d_1} & \mathbf{k}^{aa}_{d_2d_2} & \mathbf{k}^{aa}_{d_2c_2}\\ \mathbf{k}^{au}_{c_2c_1} & \mathbf{k}^{au}_{c_2d_1} & \mathbf{k}^{au}_{c_2d_2} & \mathbf{k}^{au}_{c_2c_2} & \mathbf{k}^{aa}_{c_2c_1} & \mathbf{k}^{aa}_{c_2d_1} & \mathbf{k}^{aa}_{c_2d_2} & \mathbf{k}^{aa}_{c_2c_2}\end{bmatrix}, \tag{32}$$

$$\mathbf{k}^e_{c_2d_2d_3c_3}=\begin{bmatrix}\mathbf{0} & \mathbf{0} & \mathbf{0} & \mathbf{0} & \mathbf{0} & \mathbf{0}\\ \mathbf{k}^{uu}_{d_2c_2} & \mathbf{k}^{uu}_{d_2d_2} & \mathbf{k}^{uu}_{d_2d_3} & \mathbf{k}^{uu}_{d_2c_3} & \mathbf{k}^{ua}_{d_2c_2} & \mathbf{k}^{ua}_{d_2d_2}\\ \mathbf{k}^{uu}_{d_3c_2} & \mathbf{k}^{uu}_{d_3d_2} & \mathbf{k}^{uu}_{d_3d_3} & \mathbf{k}^{uu}_{d_3c_3} & \mathbf{k}^{ua}_{d_3c_2} & \mathbf{k}^{ua}_{d_3d_2}\\ \mathbf{0} & \mathbf{0} & \mathbf{0} & \mathbf{0} & \mathbf{0} & \mathbf{0}\\ \mathbf{k}^{au}_{c_2c_2} & \mathbf{k}^{au}_{c_2d_2} & \mathbf{k}^{au}_{c_2d_3} & \mathbf{k}^{au}_{c_2c_3} & \mathbf{k}^{aa}_{c_2c_2} & \mathbf{k}^{aa}_{c_2d_2}\\ \mathbf{k}^{au}_{d_2c_2} & \mathbf{k}^{au}_{d_2d_2} & \mathbf{k}^{au}_{d_2d_3} & \mathbf{k}^{au}_{d_2c_3} & \mathbf{k}^{aa}_{d_2c_2} & \mathbf{k}^{aa}_{d_2d_2}\end{bmatrix}, \tag{33}$$

$$\mathbf{k}^e_{c_3d_3d_4c_4}=\begin{bmatrix}\mathbf{0} & \mathbf{0} & \mathbf{0} & \mathbf{0}\\ \mathbf{k}^{uu}_{d_3c_3} & \mathbf{k}^{uu}_{d_3d_3} & \mathbf{k}^{uu}_{d_3d_4} & k^{uu}_{d_3c_4}\\ \mathbf{k}^{uu}_{d_4c_3} & \mathbf{k}^{uu}_{d_4d_3} & \mathbf{k}^{uu}_{d_4d_4} & \mathbf{k}^{uu}_{d_4c_4}\\ \mathbf{0} & \mathbf{0} & \mathbf{0} & \mathbf{0}\end{bmatrix}. \tag{34}$$

And the mass matrices for element 4, element 5 and element 6 are shown as Eqs. (35)–(37), respectively.

$$\mathbf{m}^e_{c_1d_1d_2c_2}=\mathrm{diag}\left\{\mathbf{0},\mathbf{m}^u_{d_1},\mathbf{m}^u_{d_2},0,\mathbf{m}^a_{c_1},\mathbf{m}^a_{d_1},\mathbf{m}^a_{d_2},\mathbf{m}^a_{c_2}\right\}, \tag{35}$$

$$\mathbf{m}^e_{c_2d_2d_3c_3}=\mathrm{diag}\left\{\mathbf{0},\mathbf{m}^u_{d_2},\mathbf{m}^u_{d_3},\mathbf{0},\mathbf{m}^a_{c_2},\mathbf{m}^a_{d_2}\right\}, \tag{36}$$

$$\mathbf{m}^e_{c_3d_3d_4c_4}=\mathrm{diag}\left\{\mathbf{0},\mathbf{m}^u_{d_3},\mathbf{m}^u_{d_4},\mathbf{0}\right\}. \tag{37}$$

Then, the global stiffness/mass matrices are obtained by assembling the stiffness/mass matrices of all PD nodes (in regions Ω_1 and Ω_2) and element stiffness/mass matrices of all XFEs (in regions Ω_2 and Ω_3). The motion equation of coupling model of XFEM and PD can be written as

$$\mathbf{M}\ddot{\boldsymbol{\delta}}+\mathbf{K}\boldsymbol{\delta}=\mathbf{Fm}, \tag{38}$$

where $\boldsymbol{\delta}$ and $\mathbf{F}$ are displacement/enrichment variables and the load vector. $\mathbf{M}$ and $\mathbf{K}$ represent the global mass matrix and the global stiffness matrix.

5. Newmark explicit integration scheme

The Newmark explicit integration method [56,57] is adopted to study the coupling method of XFEM/PD in the present study and the Newmark explicit integration scheme is reported listed as follows:

1. Selecting the time step Δt and parameters α, β. Computing integral constants

$$A_1=\frac{1}{\alpha\Delta t^2},\ A_2=\frac{1}{\alpha\Delta t},\ A_3=\left(\frac{1}{2\alpha}-1\right)$$

2. Computing global stiffness matrix $\mathbf{K}$ and global mass matrix $\mathbf{M}$.
3. Computing $\ddot{\boldsymbol{\delta}}_0$ in the initial: $\ddot{\boldsymbol{\delta}}_0=\mathbf{M}^{-1}(\mathbf{F}-\mathbf{K}\boldsymbol{\delta}_0)$
4. Computing the effective stiffness matrix $\bar{\mathbf{K}}=\mathbf{K}+\mathbf{A}_1\mathbf{M}$
5. For each time increment,
   (1) Computing damage of all PD nodes.
   (2) Computing global stiffness matrix $\mathbf{K}$ and the effective stiffness matrix $\bar{\mathbf{K}}=\mathbf{K}+\mathbf{A}_1\mathbf{M}$, if new damage occurs.
   (3) Computing the effective loading vector $\bar{\mathbf{F}}_{t+\Delta t}$ at the moment $t+\Delta t$
   $\bar{\mathbf{F}}_{t+\Delta t}=\mathbf{F}_{t+\Delta t}+[A_1\boldsymbol{\delta}_t+A_2\dot{\boldsymbol{\delta}}_t+A_3\ddot{\boldsymbol{\delta}}_t]\mathbf{M}$
   (4) Computing the displacement vector $\boldsymbol{\delta}_{t+\Delta t}$ at the moment $t+\Delta t$
   $\boldsymbol{\delta}_{t+\Delta t}=\bar{\mathbf{K}}^{-1}\bar{\mathbf{F}}_{t+\Delta t}$
   (5) Computing the velocity and acceleration vector at the moment $t+\Delta t$

$$\ddot{\boldsymbol{\delta}}_{t+\Delta t}=\frac{1}{\alpha\Delta t^2}(\boldsymbol{\delta}_{t+\Delta t}-\boldsymbol{\delta}_t)-\frac{1}{\alpha\Delta t}\dot{\boldsymbol{\delta}}_t-(\frac{1}{2\alpha}-1)\ddot{\boldsymbol{\delta}}_t$$

$$\dot{\boldsymbol{\delta}}_{t+\Delta t}=\dot{\boldsymbol{\delta}}_t+(1-\beta)\Delta t\ddot{\boldsymbol{\delta}}_t+\beta\Delta t\ddot{\boldsymbol{\delta}}_{t+\Delta t}$$

The unconditionally stable scheme of the Newmark scheme is

$$0.5\leqslant\beta\leqslant 2\alpha. \tag{39}$$

In the present study, $\alpha=0.25$, $\beta=0.5$.

6. Numerical examples

To validate the proposed coupling method, dynamic crack propagation and branching of the rectangle plate and crack propagation of a plate with two parallel notches are studied in the present study.

6.1. Dynamic crack propagation and branching of the rectangle plate

A pre-crack plate in the plane stress state is taken into accounted, whose length L, width D, and thickness are 0.1 m, 0.04 m and 0.001 m. The plate is made of Duran 50 glass, whose properties are listed in Table 1. For bond-based PD, the Poisson's ratio is limited to 1/3 (for 2D

Table 1
The mechanical parameters of Duran 50 glass and Soda-lime glass [60].

Material	Density (ρ) (t/mm^3)	Elastic modulus (E) (MPa)	Poisson's ratio (ν)	Fracture energy (G_{IC}) (mJ/mm^2)
Duran 50 glass	2.235e−9	65000.0	0.2	0.204
Soda-lime glass	2.44e−9	72000.0	0.22	0.135

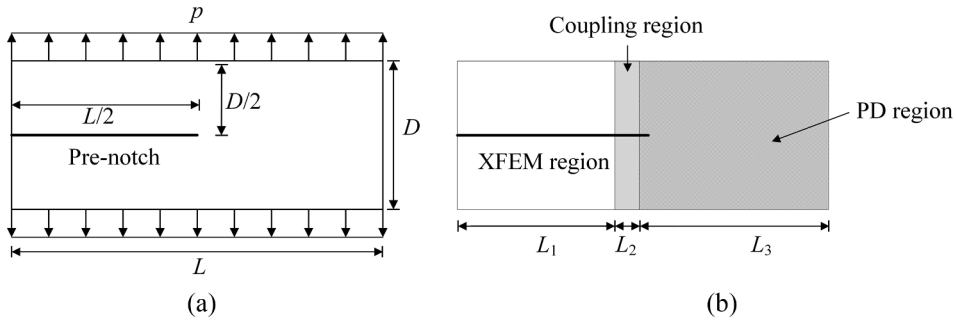

Fig. 4. Geometry model and region divisions of the rectangle plate, (a) geometry model, and (b) region divisions.

plane stress problem). Poisson's ratio has little influence on the crack propagation speed and crack propagation path [58,59]. In the present study, the Poisson ratio $\nu = 1/3$ is adopted. A uniform tensile stress $p = 12$ MPa is as shown in Fig. 4(a). The nodes of δ layers near boundaries are set as no-failure zones to prevent tearing nodes by the abrupt load. The time step and the time duration are 25 ns and 46 μs. The initial crack is introduced by removing all bonds between PD nodes through the crack line [60]. Fig. 4(b) exhibits PD region, coupling region and XFE region and the length of the above three regions are L_1, L_2 and L_3. The coupling region contains m layers PD nodes and 1 layer XFE nodes, where $m = 4$ is adopted in this study. The length of the coupling region is only depended on Δx (the spacing between two adjacent nodes).

6.1.1. Numerical convergence and computation time

The δ-convergence, as defined in Refs. [60,61], of the proposed coupling model are studied by simulating dynamic crack propagation and branching of the rectangle plate with an initial edge notch. The same calculation model has been studied in Refs. [34,60,62–65] and experiment measurement by Ref. [66]. The size of horizon δ has a great influence on results [60]. However, a series of studies have shown that $\delta \geqslant 3\Delta x$ can satisfy the computational accuracy [7,59,64]. $\delta = 4\Delta x$ is adopted in this study.

The influence of δ is investigated by using the following three cases.

Case 1: $\delta = 4.0$ mm, $\Delta x = 1.0$ mm, $m = 4$,
Case 2: $\delta = 2.0$ mm, $\Delta x = 0.5$ mm, $m = 4$,
Case 3: $\delta = 1.0$ mm, $\Delta x = 0.25$ mm, $m = 4$.

All models have the uniform grid spacing. For all cases, Lengths of PD region, coupling region and XFE region are given by Table 2. The amount of PD nodes, XFE nodes and completely cut elements of the above three cases are shown in Table 3. Fig. 5 indicated that the crack paths for all cases are almost identical to each other, the crack is initially split into two cracks nearby 71 mm distance the left boundary. The crack tips are located nearby 94 mm distance the left boundary when $t = 46$ μs.

Table 2
Lengths of PD region, coupling region and XFE region.

	Length of L_1 (mm)	Length of L_2 (mm)	Length of L_3 (mm)
Case 1	45	5	50
Case 2	45.5	2.5	52
Case 3	45.75	1.25	53

Table 3
Number of PD nodes, XFE nodes and completely cut elements.

	PD nodes	XFEM nodes	Completely cut elements
Case 1	2160	1840	47
Case 2	8640	7360	93
Case 3	34,560	29,440	185

The computation time of the PD model and coupling model for Case 3 are compared to verify the computation efficiency of the proposed coupling method of PD and XFEM. The PD model has 64,000 nodes for Case 3. The computation time and the crack paths of the above two models are shown in Table 4. It is indicated that the proposed coupling model can largely reduce the computation effort in comparison of pure PD model. In addition, crack paths for them are almost identical to each other. The hardware features of the computer are same as that list in Ref. [67].

6.1.2. Crack propagation speed

The crack propagation speed is one of the major parameters to estimate the dynamic fracture. The size and the division region of the model are the same with the example in Section 6.1. The traction loadings as shown in Fig. 4(a) is $p = 14$ MPa. The time step and the time duration are 25 ns and 40 μs. The plate is made of Soda-lime glass, whose properties are shown in Table 1. The crack propagation speed [60] is defined as

$$v_l = \frac{\|\mathbf{x}_l - \mathbf{x}_{l-1}\|}{t_l - t_{l-1}}, \tag{40}$$

where x_l and x_{l-1} represent the crack-tip positions at t_l and t_{l-1}. The data-dump is $t_l - t_{l-1} = 2$ μs. The coordinates of the crack-tip is represented by the coordinates of the right-most node, whose local damage is larger than or equal to 35%.

Three cases as below are used to study that the effect of the adjacent node space on the crack propagation speed of the proposed coupling model.

Case 1: $\delta = 4.0$ mm, $\Delta x = 1.0$ mm, $m = 4$,
Case 2: $\delta = 2.0$ mm, $\Delta x = 0.5$ mm, $m = 4$,
Case 3: $\delta = 1.0$ mm, $\Delta x = 0.25$ mm, $m = 4$.

Fig. 6 displayed the crack paths of the above three cases. The shape of the crack path of Case 1 is slightly difference compared with Case 2

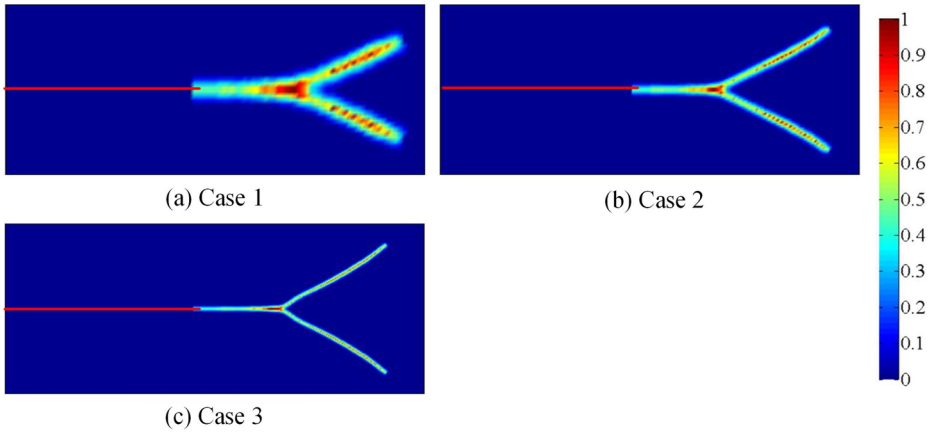

Fig. 5. Crack propagation and branching paths with different δ, (a) Case 1, (b) Case 2, and (c) Case 3.

Table 4
CPU computation time and crack paths for different models.

Model	PD	PD/XFEM
Computation time (s)	10,995	6518
Crack path	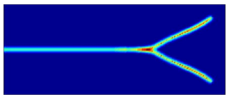	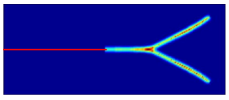

and Case 3, but the paths of Case 2 and Case 3 look almost identical to one another. The initiation of crack branching of the above three cases are close to 0.068 m, and the crack path angle has a slight turn near 0.08 m from the left-side of the plate.

Fig. 7 shows the crack propagation speeds for the above three cases. The fluctuations of the crack propagation speeds decrease with the decrease of the adjacent nodes space Δx.

The crack propagation path corresponding to Case 3 obtained by the proposed method and the PD result in Ref. [60] are shown in Fig. 8, which indicated that the crack paths of the above models are good agreement with each other.

Fig. 9 gives the crack propagation speed corresponding to Case 3 obtained by the proposed method in comparison with the result in Ref. [60]. There exists small drops of the curves around 16 μs and 22 μs. The crack propagation speed of the proposed method agree well with that of Ref. [60]. The maximum crack propagation speeds for the proposed coupling method, the result in Ref. [60] and the experiment measurement [66] are around 1736 m/s, 1681 m/s and 1580 m/s, respectively. The Rayleigh wave speed [60,68] is around 3244 m/s. The maximum crack propagation speed value of the proposed coupling method is far less than the Rayleigh wave speed.

6.2. Simulation of Kalthoff-Winkler experiment

The Kalthoff-Winkler experiment [69] is a typtical crack propagation example, which has been simulated by Refs. [51,62,64,70–74]. The L and D of rectangle plate as shown in Fig. 10(a) are both equal to 0.1 m. The two parallel initial cracks with a depth of 0.05 m is located

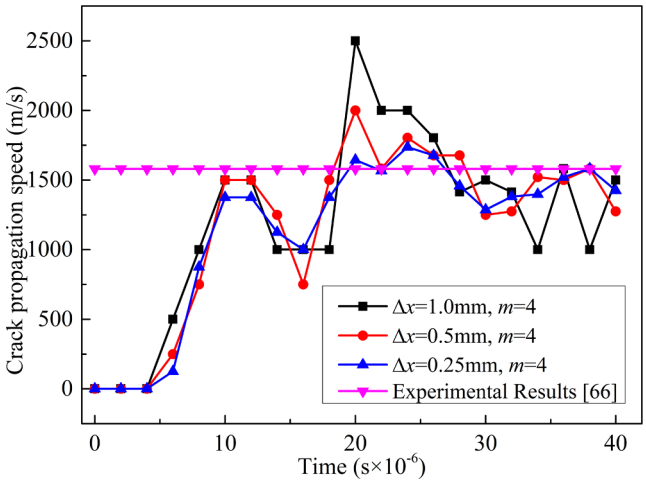

Fig. 7. Crack propagation speeds for different adjacent nodes apace.

at the left boundary of the plate. A constant speed V_0 of 16.5 m/s is applied upon the left boundary between two parallel initial cracks. The left region with the initial crack is the XFE region, and the right region with the crack tip is the PD region. As shown in Fig. 10(b), the lengths of XFEM region, coupling region and peridynamic region are $L_1 = 0.0425$ m, $L_2 = 0.0025$ m and $L_1 = 0.055$ m. The grid spacing is $\Delta x = 0.5$ mm, and there are 34,400 XFE nodes (172 completely cut elements) and 45,600 PD nodes in the model. The PD horizon is $\delta = 2.0$ mm with m equaling to 4. The mechanical parameters of material are: Young's modulus $E = 190{,}000$ MPa, Poisson's ratio $\rho = 8.0e-9$ t/mm^3, and fracture energy $G_{IC} = 22.17$ mJ/mm^2. The time step and the total time are 50 ns and 80 μs.

Fig. 11 gives the crack paths obtained by the proposed coupling model comparing with PD result of Ref. [51], which indicated that the simulated results of the coupling method of XFEM/PD agree well with PD result of Ref. [51].

The crack propagation speeds for the coupling model can be compared with that for other numerical results. The data-dumps are done every 2.5 μs. The relative crack propagation speed, V/C_R, is defined in

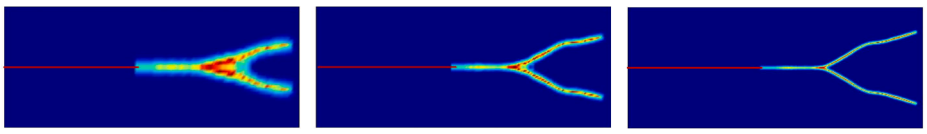

Fig. 6. Crack propagation and branching paths for different Δx, (a) Case 1, (b) Case 2, and (c) Case 3.

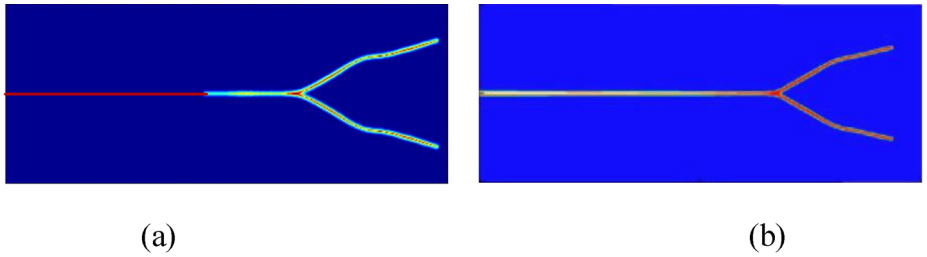

Fig. 8. The crack paths of the proposed coupling model and that in Ref. [60], (a) the proposed coupling model, and (b) PD result in Ref. [60].

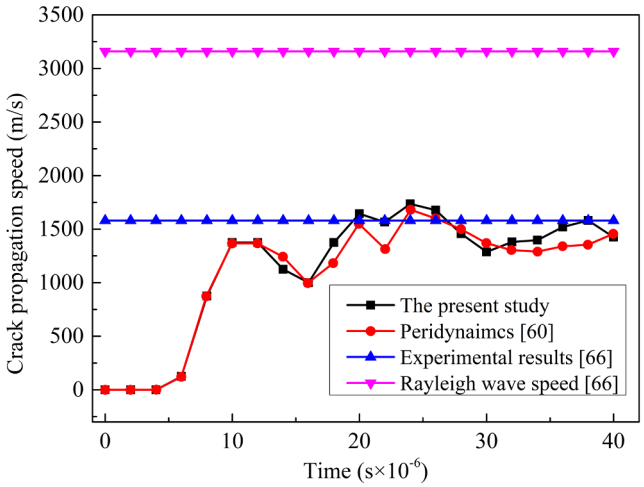

Fig. 9. Comparing crack propagation speed of the proposed method with that excerpted from Refs. [60] and [66].

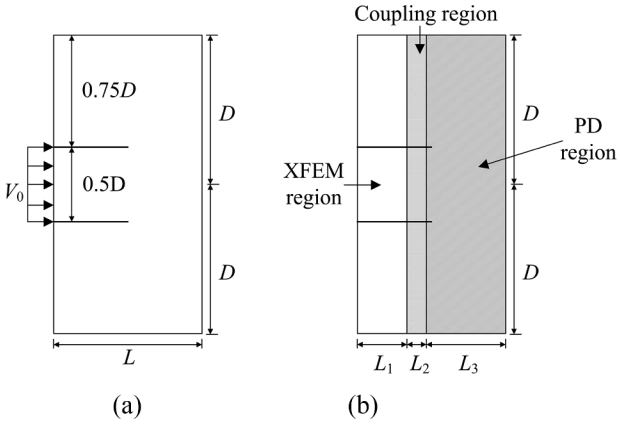

Fig. 10. Geometry model and region divisions of the rectangle plate, (a) geometry model, and (b) region divisions.

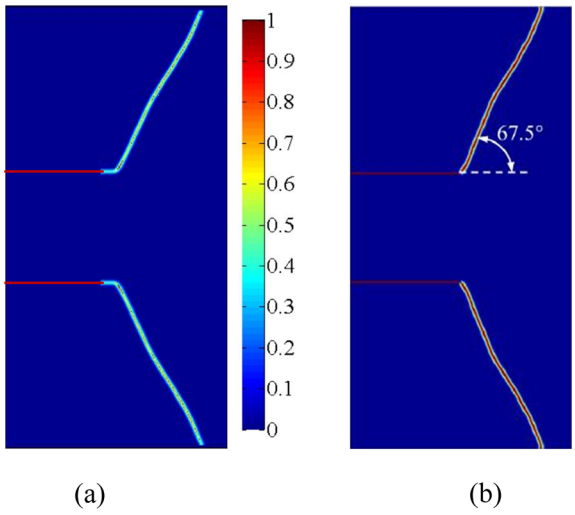

Fig. 11. Comparing the crack paths between numerical and experimental results, (a) the proposed coupling method, and (b) peridynamics in Ref.[51].

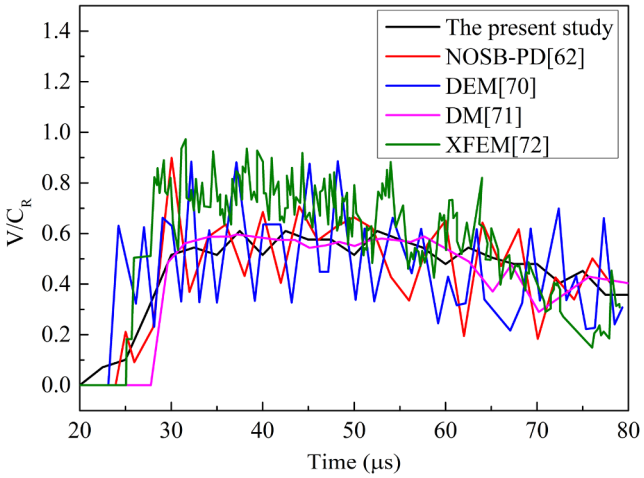

Fig. 12. Comparing crack propagation speeds with different methods.

the present study, where C_R represents the Rayleigh wave speed. Fig. 12 provides the relative crack propagation speed of the coupling method in comparison of that obtained by PD in Ref. [62], discrete element method (DEM) in Ref. [70], discrete method (DM) in Ref. [71] and XFEM in Ref. [72]. The crack propagation of the proposed coupling method starts at 22.5 μs and the propagation speed is always less than the Rayleigh wave speed. The results of the proposed coupling method of XFEM/PD agree well with results of Refs. [62,70–72].

7. Conclusions

A coupling method of extended finite element method (XFEM) and peridynamics (PD) is proposed to exert the advantages of these two numerical methods to studying the 2D dynamic crack propagation problems. The coupling method does not require the overlapping region. Numerical examples show that the crack propagation speed calcuated from the couping method trends to a stable value with the decrease the adjacent nodes space. In addition, the proposed method has both the accuracy and efficiency in solving dynamic and crack propagation and branching problems. The coupling method can be developed further in the future work using the adaptive divisions of XFE and PD regions and for 3D crack propagation problems.

Declaration of Competing Interest

The authors declare that they have no known competing financial

interests or personal relationships that could have appeared to influence the work reported in this paper.

Acknowledgement

This work was supported by the National Natural Science Foundation of China (Grant Nos. 11732002 and 11672089), the Fundamental Research Funds for the Central Universities (Grant No. HIT.NSRIF.2017017) and Natural Science Foundation of Heilongjiang Province, China (Grant No. A2017003).

References

[1] P.R.S. Antunes, S.S. Valtchev, A meshfree numerical method for acoustic wave propagation problems in planar domains with corners and cracks, J. Comput. Appl. Math. 234 (9) (2010) 2646–2662.
[2] F.L. Sun, C.Y. Dong, H.S. Yang, Isogeometric boundary element method for crack propagation based on Bézier extraction of NURBS, Eng. Anal. Bound. Elem. 99 (2019) 76–88.
[3] T. Rabczuk, J.H. Song, T. Belytschko, Simulations of instability in dynamic fracture by the cracking particles method, Eng. Fract. Mech. 76 (6) (2009) 730–741.
[4] Yu. Tiantang, Extended Finite Element Method: Theory, Applications, and Programs, Science Press, 2014.
[5] Zhuo Zhuang, Zhanli Liu, Binbin Cheng, Jianhua Liao, Extended Finite Element Method, Tsinghua University Press, 2015.
[6] S.A. Silling, Reformulation of elasticity theory for discontinuities and long-range forces, J. Mech. Phys. Solids 48 (1) (2000) 175–209.
[7] S.A. Silling, E. Askari, A meshfree method based on the peridynamic model of solid mechanics, Comput. Struct. 83 (17–18) (2005) 1526–1535.
[8] S.A. Silling, R.B. Lehoucq, Peridynamic theory of solid mechanics, Advances in Applied Mechanics vol. 44, (2010) 73–168.
[9] L. Wang, J. Xu, J. Wang, A peridynamic framework and simulation of non-Fourier and nonlocal heat conduction, Int. J. Heat Mass Transf. 118 (2018) 1284–1292.
[10] L. Wang, R. Abeyaratne, A one-dimensional peridynamic model of defect propagation and its relation to certain other continuum models, J. Mech. Phys. Solids 116 (2018) 334–349.
[11] L. Wang, J. Xu, J. Wang, Elastodynamics of linearized isotropic state-based peridynamic media, J. Elast. (2019) 1–20.
[12] L. Wang, J. Xu, J. Wang, et al., A mechanism-based spatiotemporal non-local constitutive formulation for elastodynamics of composites, Mech. Mater. 128 (2019) 105–116.
[13] B. Kilic, E. Madenci, An adaptive dynamic relaxation method for quasi-static simulations using the peridynamic theory, Theor. Appl. Fract. Mech. 53 (3) (2010) 194–204.
[14] T. Ni, M. Zaccariotto, Q.Z. Zhu, et al., Static solution of crack propagation problems in Peridynamics, Comput. Meth. Appl. Mech. Eng. 346 (2019) 126–151.
[15] Y. Wang, X. Zhou, Y. Wang, et al., A 3-D conjugated bond-pair-based peridynamic formulation for initiation and propagation of cracks in brittle solids, Int. J. Solids Struct. 134 (2018) 89–115.
[16] T. Rabczuk, H. Ren, A peridynamics formulation for quasi-static fracture and contact in rock, Eng. Geol. 225 (2017) 42–48.
[17] Y. Wang, X. Zhou, Y. Shou, The modeling of crack propagation and coalescence in rocks under uniaxial compression using the novel conjugated bond-based peridynamics, Int. J. Mech. Sci. 128–129 (2017) 614–643.
[18] Y. Shou, X. Zhou, F. Berto, 3D numerical simulation of initiation, propagation and coalescence of cracks using the extended non-ordinary state-based peridynamics, Theor. Appl. Fract. Mech. 101 (2019) 254–268.
[19] X. Lai, L. Liu, S. Li, et al., A non-ordinary state-based peridynamics modeling of fractures in quasi-brittle materials, Int. J. Impact Eng. 111 (2018) 130–146.
[20] R.W. Liu, Y.Z. Xue, X.K. Lu, et al., Simulation of ship navigation in ice rubble based on peridynamics, Ocean Eng. 148 (2018) 286–298.
[21] Y. Wang, X. Zhou, X. Xu, Numerical simulation of propagation and coalescence of flaws in rock materials under compressive loads using the extended non-ordinary state-based peridynamics, Eng. Fract. Mech. 163 (2016) 248–273.
[22] Y.T. Wang, X.P. Zhou, M.M. Kou, Three-dimensional numerical study on the failure characteristics of intermittent fissures under compressive-shear loads, Acta Geotech. 14 (4) (2019) 1161–1193.
[23] H. Ren, X. Zhuang, T. Rabczuk, Implementation of gtn model in dual-horizon peridynamics, Proc. Eng. 197 (2017) 224–232.
[24] H. Ren, X. Zhuang, T. Rabczuk, Dual-horizon peridynamics: A stable solution to varying horizons, Comput. Meth. Appl. Mech. Eng. 318 (2017) 762–782.
[25] S. Rokkam, M. Gunzburger, M. Brothers, et al., A nonlocal peridynamics modeling approach for corrosion damage and crack propagation, Theor. Appl. Fract. Mech. 101 (2019) 373–387.
[26] Z.Q. Cheng, Z.B. Sui, H. Yin, et al., Studies of dynamic fracture in functionally graded materials using peridynamic modeling with composite weighted bond, Theor. Appl. Fract. Mech. 103 (2019) 102242.
[27] M.M. Kou, Y.J. Lian, Y.T. Wang, Numerical investigations on crack propagation and crack branching in brittle solids under dynamic loading using bond-particle model, Eng. Fract. Mech. 212 (2019) 41–56.
[28] X. Zhou, Y. Wang, Y. Shou, et al., A novel conjugated bond linear elastic model in bond-based peridynamics for fracture problems under dynamic loads, Eng. Fract. Mech. 188 (2018) 151–183.
[29] S.A. Silling, M.L. Parks, J.R. Kamm, et al., Modeling shockwaves and impact phenomena with Eulerian peridynamics, Int. J. Impact Eng. 107 (2017) 47–57.
[30] Y. Wang, X. Zhou, M. Kou, An improved coupled thermo-mechanic bond-based peridynamic model for cracking behaviors in brittle solids subjected to thermal shocks, Eur. J. Mech.-A/Solids 73 (2019) 282–305.
[31] E. Madenci, A. Barut, M. Futch, Peridynamic differential operator and its applications, Comput. Meth. Appl. Mech. Eng. 304 (2016) 408–451.
[32] M. Nowruzpour, J.N. Reddy, Unification of local and nonlocal models within a stable integral formulation for analysis of defects, Int. J. Eng. Sci. 132 (2018) 45–59.
[33] S. Sarkar, M. Nowruzpour, J.N. Reddy, et al., A discrete Lagrangian based direct approach to macroscopic modelling, J. Mech. Phys. Solids 98 (2017) 172–180.
[34] A. Shojaei, T. Mudric, M. Zaccariotto, et al., A coupled meshless finite node/Peridynamic method for 2D dynamic fracture analysis, Int. J. Mech. Sci. 119 (2016) 419–431.
[35] B. Kilic, E. Madenci, Coupling of peridynamic theory and the finite element method, J. Mech. Mater. Struct. 5 (5) (2010) 707–733.
[36] P. Seleson, S. Beneddine, S. Prudhomme, A force-based coupling scheme for peridynamics and classical elasticity, Comput. Mater. Sci. 66 (2013) 34–49.
[37] J. Lee, W. Liu, J.W. Hong, Impact fracture analysis enhanced by contact of peridynamic and finite element formulations, Int. J. Impact Eng. 87 (2016) 108–119.
[38] R.W. Macek, S.A. Silling, Peridynamics via finite element analysis, Finite Elem. Anal. Des. 43 (15) (2007) 1169–1178.
[39] W. Liu, J.W. Hong, A coupling approach of discretized peridynamics with finite element method, Comput. Meth. Appl. Mech. Eng. 245 (2012) 163–175.
[40] E. Oterkus, A. Barut, E. Madenci, Damage growth prediction from loaded composite fastener holes by using peridynamic theory, 51st AIAA/ASME/ASCE/AHS/ASC Structures, Structural Dynamics, and Materials Conference 18th AIAA/ASME/AHS Adaptive Structures Conference 12th, 2010, p. 3026.
[41] E. Oterkus, E. Madenci, O. Weckner, et al., Combined finite element and peridynamic analyses for predicting failure in a stiffened composite curved panel with a central slot, Compos. Struct. 94 (3) (2012) 839–850.
[42] G. Lubineau, Y. Azdoud, F. Han, et al., A morphing strategy to couple non-local to local continuum mechanics, J. Mech. Phys. Solids 60 (6) (2012) 1088–1102.
[43] F. Han, G. Lubineau, Coupling of nonlocal and local continuum models by the Arlequin approach, Int. J. Num. Meth. Eng. 89 (6) (2012) 671–685.
[44] Y. Azdoud, F. Han, G. Lubineau, A morphing framework to couple non-local and local anisotropic continua, Int. J. Solids Struct. 50 (9) (2013) 1332–1341.
[45] Y. Azdoud, F. Han, G. Lubineau, The morphing method as a flexible tool for adaptive local/non-local simulation of static fracture, Comput. Mech. 54 (3) (2014) 711–722.
[46] F. Han, G. Lubineau, Y. Azdoud, et al., A morphing approach to couple state-based peridynamics with classical continuum mechanics, Comput. Meth. Appl. Mech. Eng. 301 (2016) 336–358.
[47] F. Han, G. Lubineau, Y. Azdoud, Adaptive coupling between damage mechanics and peridynamics: a route for objective simulation of material degradation up to complete failure, J. Mech. Phys. Solids 94 (2016) 453–472.
[48] U. Galvanetto, T. Mudric, A. Shojaei, et al., An effective way to couple FEM meshes and Peridynamics grids for the solution of static equilibrium problems, Mech. Res. Commun. 76 (2016) 41–47.
[49] A. Shojaei, M. Zaccariotto, U. Galvanetto, Coupling of 2D discretized Peridynamics with a meshless method based on classical elasticity using switching of nodal behaviour, Eng. Comput. 34 (5) (2017) 1334–1366.
[50] M. Zaccariotto, D. Tomasi, U. Galvanetto, An enhanced coupling of PD grids to FE meshes, Mech. Res. Commun. 84 (2017) 125–135.
[51] M. Zaccariotto, T. Mudric, D. Tomasi, et al., Coupling of FEM meshes with Peridynamic grids, Comput. Meth. Appl. Mech. Eng. 330 (2018) 471–497.
[52] T. Belytschko, T. Black, Elastic crack growth in finite elements with minimal remeshing, Int. J. Num. Meth. Eng. 45 (5) (1999) 601–620.
[53] N. Moës, J. Dolbow, T. Belytschko, A finite element method for crack growth without remeshing, Int. J. Num. Meth. Eng. 46 (1) (1999) 131–150.
[54] K. Ravi-Chandar, Dynamic Fracture, Elsevier, 2004.
[55] E. Madenci, E. Oterkus, Peridynamic Theory and its Applications, Springer, New York, 2014.
[56] T. Menouillard, J. Rethore, A. Combescure, et al., Efficient explicit time stepping for the eXtended Finite Element Method (X-FEM), Int. J. Num. Meth. Eng. 68 (9) (2006) 911–939.
[57] Xu. Bin, Yuefei Gao, Yu Long, Finite Element Structure Dynamics Analysis and Engineering Application, Tsinghua University Press, 2009.
[58] F. Delale, F. Erdogan, The crack problem for a nonhomogeneous plane, J. Appl. Mech. 50 (3) (1983) 609–614.
[59] Z. Cheng, G. Zhang, Y. Wang, et al., A peridynamic model for dynamic fracture in functionally graded materials, Compos. Struct. 133 (2015) 529–546.
[60] Y.D. Ha, F. Bobaru, Studies of dynamic crack propagation and crack branching with peridynamics, Int. J. Fract. 162 (1–2) (2010) 229–244.
[61] F. Bobaru, M. Yang, L.F. Alves, et al., Convergence, adaptive refinement, and scaling in 1D peridynamics, Int. J. Num. Meth. Eng. 77 (6) (2009) 852–877.
[62] X. Zhou, Y. Wang, Q. Qian, Numerical simulation of crack curving and branching in brittle materials under dynamic loads using the extended non-ordinary state-based peridynamics, Eur. J. Mech.-A/Solids 60 (2016) 277–299.
[63] Y.D. Ha, F. Bobaru, Characteristics of dynamic brittle fracture captured with peridynamics, Eng. Fract. Mech. 78 (6) (2011) 1156–1168.
[64] D. Dipasquale, M. Zaccariotto, U. Galvanetto, Crack propagation with adaptive grid refinement in 2D peridynamics, Int. J. Fract. 190 (1–2) (2014) 1–22.
[65] J.H. Song, H. Wang, T. Belytschko, A comparative study on finite element methods

for dynamic fracture, Comput. Mech. 42 (2) (2008) 239–250.
[66] G. Fang, S. Liu, M. Fu, et al., A method to couple state-based peridynamics and finite element method for crack propagation problem, Mech. Res. Commun. 95 (2019) 89–95.
[67] F.P. Bowden, J.H. Brunton, J.E. Field, et al., Controlled fracture of brittle solids and interruption of electrical current, Nature 216 (5110) (1967) 38.
[68] K.F. Graff, Wave Motion in Elastic Solids, Publication of: Oxford University Press, 1975.
[69] J.F. Kalthoff, S. Winkler, Failure mode transition at high rates of shear loading. DGM Informationsgesellschaft mbH, Imp. Load. Dyn. Behav. Mater. 1 (1988) 185–195.
[70] L. Kosteski, R.B. D'Ambra, I. Iturrioz, Crack propagation in elastic solids using the truss-like discrete element method, Int. J. Fract. 174 (2) (2012) 139–161.
[71] M. Braun, J. Fernández-Sáez, A new 2D discrete model applied to dynamic crack propagation in brittle materials, Int. J. Solids Struct. 51 (21–22) (2014) 3787–3797.
[72] T. Belytschko, H. Chen, J. Xu, et al., Dynamic crack propagation based on loss of hyperbolicity and a new discontinuous enrichment, Int. J. Num. Meth. Eng. 58 (12) (2003) 1873–1905.
[73] A.E. Huespe, J. Oliver, P.J. Sanchez, et al., Strong discontinuity approach in dynamic fracture simulations, Mecánica Computacional 25 (2006) 1997–2018.
[74] Y.H. Bie, X.Y. Cui, Z.C. Li, A coupling approach of state-based peridynamics with node-based smoothed finite element method, Comput. Meth. Appl. Mech. Eng. 331 (2018) 675–700.